



## Electronic structure of the intermediate-valence compound $\text{EuNi}_2\text{P}_2$ studied by soft x-ray photoemission spectroscopy

Ikuto Kawasaki <sup>1,\*</sup>, Masaaki Kobata,<sup>1</sup> Shin-ichi Fujimori,<sup>1</sup> Yukiharu Takeda,<sup>1</sup> Hiroshi Yamagami <sup>1,2</sup>, Masato Hedo,<sup>3</sup> Takao Nakama,<sup>3</sup> and Yoshichika Onuki<sup>3,4</sup>

<sup>1</sup>Materials Sciences Research Center, Japan Atomic Energy Agency, Sayo, Hyogo 679-5148, Japan

<sup>2</sup>Department of Physics, Faculty of Science, Kyoto Sangyo University, Kyoto 603-8555, Japan

<sup>3</sup>Faculty of Science, University of the Ryukyus, Nishihara, Okinawa 903-0213, Japan

<sup>4</sup>RIKEN Center for Emergent Matter Science, Wako, Saitama 351-0198, Japan



(Received 1 December 2020; revised 7 September 2021; accepted 20 September 2021; published 12 October 2021)

We carried out angle-resolved photoemission (ARPES) experiments using soft x rays to investigate the electronic structure of the intermediate-valence compound  $\text{EuNi}_2\text{P}_2$ . Both the  $\text{Eu}^{2+}$  and  $\text{Eu}^{3+}$  components arising from the  $4f^6$  and  $4f^5$  final states were observed in the valence spectra, directly confirming an intermediate-valence character of Eu ions. The three-dimensional band structure was studied by ARPES measurements, and the ARPES results were compared with calculations based on the density-functional theory for the non- $4f$  reference compounds  $\text{SrNi}_2\text{P}_2$  and  $\text{YNi}_2\text{P}_2$ . We found that the ARPES spectra up to just below the Fermi level are better reproduced by the calculation of  $\text{SrNi}_2\text{P}_2$  rather than that of  $\text{YNi}_2\text{P}_2$ . The heavy-fermion bands in  $\text{EuNi}_2\text{P}_2$  are thus considered to be formed through the hybridization between the dispersive valence bands, which resemble those for  $\text{SrNi}_2\text{P}_2$ , and the  $\text{Eu}^{2+}$  components located at the very vicinity of the Fermi level.

DOI: [10.1103/PhysRevB.104.165124](https://doi.org/10.1103/PhysRevB.104.165124)

### I. INTRODUCTION

Intermetallic compounds with rare-earth elements have drawn considerable attention since they exhibit a variety of intriguing properties, such as heavy-fermion state, non-Fermi-liquid behavior, and unconventional superconductivity. These phenomena are ascribed to the complex many-body interaction between localized  $4f$  electrons and conduction electrons. Recently, it has been pointed out that unconventional superconductivity and non-Fermi-liquid behavior in some Ce- and Yb-based compounds are associated with the valence instability [1–4]. Hence, understanding the nature of valence fluctuations in these compounds and their electronic structures is an important issue among the  $f$ -electron physics.

It has been reported that some Eu-based compounds show valence instability, and their valence states can be tuned by external parameters, such as pressure, temperature, and chemical substitution [5]. This valence instability is ascribed to the small energy difference between the magnetic  $\text{Eu}^{2+}$  state ( $4f^7$ :  $S = 7/2$ ,  $L = 0$ , and  $J = 7/2$ ) and the nonmagnetic  $\text{Eu}^{3+}$  state ( $4f^6$ :  $S = 3$ ,  $L = 3$ , and  $J = 0$ ). Here,  $S$ ,  $L$ , and  $J$  represent the spin, orbital, and total angular momentum, respectively. Valence transitions have actually been observed in several Eu compounds, such as  $\text{EuRh}_2\text{Si}_2$  [6,7],  $\text{EuNi}_2\text{Ge}_2$  [8,9],  $\text{EuCo}_2\text{Ge}_2$  [10], and  $\text{EuGa}_4$  [11]; these compounds have nearly divalent valence states and show antiferromagnetic order at low temperatures. They exhibit pressure-induced valence transitions to a nearly  $\text{Eu}^{3+}$  state. Their magnetic ordered states due to  $\text{Eu}^{2+}$  ions abruptly disappear at critical pressure, at which valence transitions occur, and above

the critical pressure, these compounds exhibit first-order temperature-induced valence transitions. Therefore, their  $P$ - $T$  phase diagrams are markedly different from those of Ce- and Yb-based heavy-fermion systems.

Recently, it has been found that there exists another type of Eu compounds whose pressure variation of the magnetic ordering temperature resembles the Doniach phase diagram as in Ce- and Yb-based compounds [12]. For example,  $\text{Eu}_2\text{Ni}_3\text{Ge}_5$  and  $\text{EuRhSi}_3$  are reported to belong to this type [13]. The Néel temperature of  $\text{Eu}_2\text{Ni}_3\text{Ge}_5$  ( $T_N = 19$  K) initially increases with pressure up to around 7 GPa and then decreases continuously toward zero with further increasing pressure.  $\text{EuRhSi}_3$  exhibits similar behavior. As another example, the phase diagram of  $\text{EuCu}_2(\text{Ge}_{1-x}\text{Si}_x)_2$  is also similar to the Doniach phase diagram [14–16]. In these compounds, the Eu valence is therefore considered to evolve continuously upon increasing pressure and doping, and interestingly heavy-fermion behavior is observed in the thermodynamic and transport measurements at around the critical pressure and concentration at which  $T_N$  drops to zero.

Among the Eu-based compounds,  $\text{EuNi}_2\text{P}_2$  is particularly interesting since it exhibits intermediate valence as well as heavy-fermion behavior at ambient pressure. The Eu valence weakly depends on temperature and is estimated to be around 2.5 at low temperatures by Mössbauer experiments [17]. The various physical quantities, such as electrical resistivity, specific heat, and nuclear spin-lattice relaxation rate, exhibit Fermi-liquid behavior at low temperatures without any sign of magnetic ordering [18–20]. The electronic specific heat coefficient is estimated to be  $\gamma \sim 100$  mJ K<sup>-2</sup> mol<sup>-1</sup>, reflecting highly enhanced effective masses of quasiparticles [18,19]. The ratio of the observed  $\gamma$  value and the quadratic term in the resistivity fulfills the generalized Kadowaki-Woods plot

\*kawasaki.ikuto@jaea.go.jp

with  $N = 4$  [21]. In addition, the temperature dependence of electrical resistivity and thermal expansion is similar to that of Ce-based heavy-fermion compounds, indicating that the formation of the heavy-fermion state is associated with the Kondo effect [18,22].

The electronic structure of  $\text{EuNi}_2\text{P}_2$  has been studied by high-resolution angle-resolved photoemission (ARPES) experiments using low-energy photons ( $h\nu = 34$  to  $70$  eV) [23,24]. These ARPES studies directly observed splittings and dispersions of the  $4f$  final state multiplet components caused by the hybridization with Ni  $3d$  derived bands, revealing that the hybridization between the  $4f$  and the conduction electrons plays a key role for the heavy-fermion behavior. On the other hand, the previous ARPES experiments were performed in a limited region in the momentum space and focused on the band structure near the Fermi level ( $E_F$ ). Therefore, the entire band structure of this compound has not been fully clarified yet. In this paper, we performed ARPES experiments using bulk-sensitive soft x rays [25,26] over wider momentum and energy ranges to derive the three-dimensional band structure and further investigate the intermediate-valence state and heavy-fermion behavior in  $\text{EuNi}_2\text{P}_2$ .

## II. EXPERIMENTAL DETAILS

A single crystalline sample of  $\text{EuNi}_2\text{P}_2$  was grown by the Sn-flux method. The details of sample preparation are given in Ref. [18]. The photoemission experiments were performed at the soft x-ray undulator beamline BL23SU [27] in SPring-8. Various photon energies in the soft x-ray range (500 to 1200 eV) were used. The energy and angular distributions of photoelectrons were measured using a Gammadata-Scienta SES2002 analyzer. The energy resolutions were about 90, 130, and 280 meV for  $h\nu = 500, 700,$  and  $1200$  eV, respectively, and the angular resolution along the analyzer slit was  $\pm 0.15^\circ$ . The binding energy of the photoemission spectra was determined with respect to the Fermi edge of an evaporated gold film, and the position of ARPES scans in the momentum space was calculated using a free-electron final state model with an inner potential value of  $V_0 = 12$  eV [28]. The base pressure of the main chamber was kept better than  $2 \times 10^{-8}$  Pa, and the sample temperature was controlled by a liquid helium flow cryostat and maintained at 20 K throughout the experiments. A clean sample surface parallel to the (001) plane was obtained by cleaving *in situ* just before the measurements.

## III. RESULTS AND DISCUSSION

Figure 1(a) shows the angle-integrated photoemission (AIPES) spectrum of the  $\text{EuNi}_2\text{P}_2$  measured at  $h\nu = 500$  eV. At this photon energy, the Eu  $4f$  and Ni  $3d$  orbitals have dominant contributions because of their strong photoemission cross sections, which are more than one order of magnitude larger than those of other states, such as Eu  $5d$  and P  $3p$  [30]. The peak located at around 1.8 eV originates from Ni  $3d$  derived bands. It is generally known that  $\text{Eu}^{2+}$  components arising from the  $4f^6$  final state multiplet are usually observed between  $E_F$  and 2 eV, and  $\text{Eu}^{3+}$  components arising from the  $4f^5$  final state multiplet exist between 6 and 11 eV [15,31].

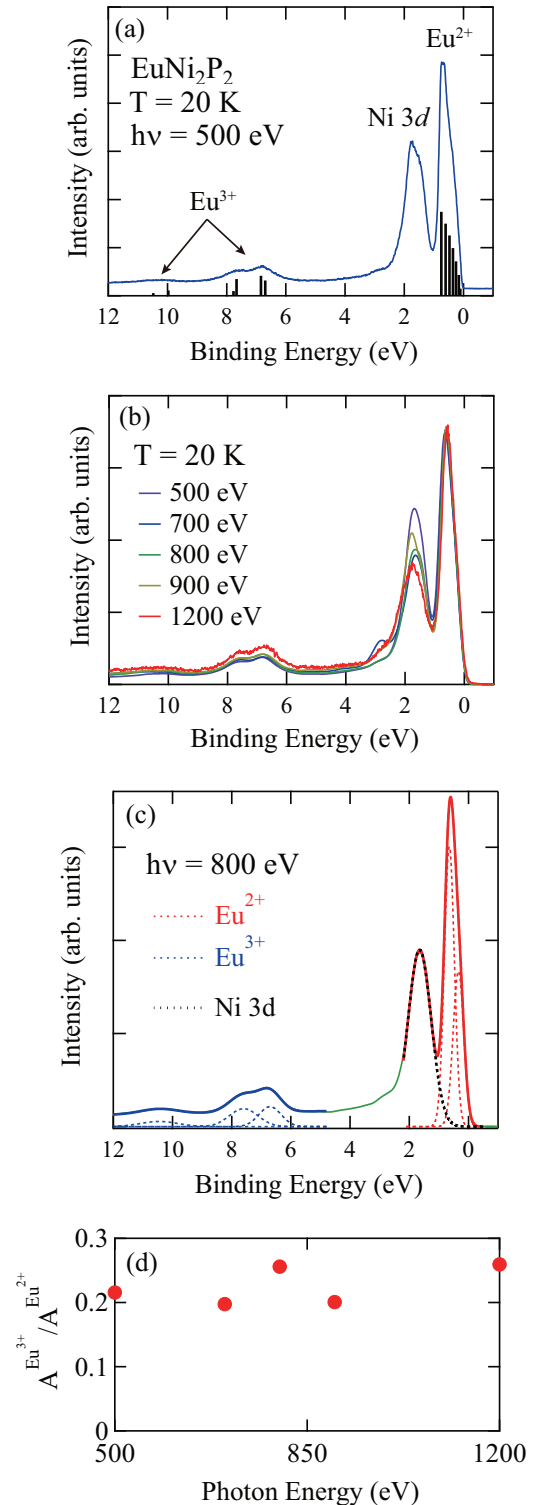


FIG. 1. (a) AIPES spectrum of  $\text{EuNi}_2\text{P}_2$  measured at  $h\nu = 500$  eV. The vertical bars show the calculated  $4f^6$  and  $4f^5$  final state multiplets cited from Refs. [15,29], which correspond to the  $\text{Eu}^{2+}$  and  $\text{Eu}^{3+}$  components, respectively. These calculated multiplets are shifted to match the experimental  $\text{Eu}^{2+}$  and  $\text{Eu}^{3+}$  peaks. (b) AIPES spectra of  $\text{EuNi}_2\text{P}_2$  measured with various photon energies ranging from 500 to 1200 eV. (c) Fitted AIPES spectrum for  $h\nu = 800$  eV. In (c), the solid red and blue lines are results of fitting, and the dashed lines represent the spectral components. (d) Photon energy dependence of the intensity ratio between  $\text{Eu}^{2+}$  and  $\text{Eu}^{3+}$  components.

Both  $\text{Eu}^{2+}$  and  $\text{Eu}^{3+}$  components are clearly observed in our spectrum, reflecting the intermediate-valence character of the Eu ions. The vertical bars represent the results of atomic calculation of the  $4f^6$  and  $4f^5$  final state multiplets [15,29]; the observed  $\text{Eu}^{2+}$  and  $\text{Eu}^{3+}$  components are well reproduced by this calculation.

Next, we argue the position of the  $\text{Eu}^{2+}$  peak. The  $\text{Eu}^{2+}$  components are considered to move toward  $E_F$  by approaching the trivalent state from the divalent state since the energy difference between  $\text{Eu}^{2+}$  and  $\text{Eu}^{3+}$  states decreases during this process. For this reason, the  $4f^6$  multiplet component with lowest binding energy for intermediate-valence compounds is considered to be located at the immediate vicinity of  $E_F$ . The position of the  $\text{Eu}^{2+}$  peak for  $h\nu = 500$  eV in Fig. 1(a) is 0.68 eV and very close to that of the nearly trivalent intermediate-valence compound  $\text{EuCu}_2\text{Si}_2$  ( $\sim 0.65$  eV) [32], suggesting that the overall positions of  $4f^6$  multiplet components are almost the same between these compounds. Therefore, the  $4f^6$  multiplet component with lowest binding energy for  $\text{EuNi}_2\text{P}_2$  seems to be located in the immediate vicinity of  $E_F$ , further supporting the intermediate-valence character of the Eu ions of  $\text{EuNi}_2\text{P}_2$ .

As seen in Fig. 1(a), the intensity of the  $\text{Eu}^{3+}$  components is much weaker than that of the  $\text{Eu}^{2+}$  components. One may consider that this result is not consistent with the Mössbauer experiments, in which the Eu valence is estimated to be  $\sim 2.5$  [17]. In fact, the intensity ratio between  $\text{Eu}^{2+}$  and  $\text{Eu}^{3+}$  is estimated to be 7:6 under the assumption that the intensities for  $\text{Eu}^{2+}$  and  $\text{Eu}^{3+}$  are simply proportional to the initial  $4f$  electron numbers and the Eu valence is 2.5. Here, we discuss the possible origins for the observed intensity ratio between  $\text{Eu}^{2+}$  and  $\text{Eu}^{3+}$  components. It is known that the Eu ions in the surface layer often have a divalent state [15,29], and the intensity of  $\text{Eu}^{2+}$  components could be enhanced by the divalent Eu ions in the surface region. Moreover, recent photoelectron diffraction experiments performed on the intermediate-valence compound  $\text{EuIr}_2\text{Si}_2$ , which is isostructural with  $\text{EuNi}_2\text{P}_2$ , have revealed that there are two different terminations for  $\text{EuIr}_2\text{Si}_2$ : Eu and Si terminated ones and that for the Si-terminated surfaces, there exist substantial deviations of the Eu valence values from the bulk value not only in the first subsurface Eu layer (fourth atomic layer below the surface) but also in the next deeper lying Eu layer (eighth atomic layer below the surface) [33]. This study implies that the valence values for Eu ions in the surface and subsurface regions may deviate from that for the bulk region.

If there is a similar shift of the Eu valency in the subsurface region for  $\text{EuNi}_2\text{P}_2$ , the intensity ratio between  $\text{Eu}^{2+}$  and  $\text{Eu}^{3+}$  components should depend on the incident photon energy since the photoelectron mean free path  $\lambda$  increases with photon energy. Here, we define the subsurface region as one unit cell below the surface because all of the above Eu layers of  $\text{EuIr}_2\text{Si}_2$ , whose valence value deviates from the bulk value, are in this region. Therefore, the thickness of the subsurface region ( $d$ ) for  $\text{EuNi}_2\text{P}_2$  corresponds to the lattice constant for the  $c$  axis ( $\sim 9.5$  Å [34]). We consider that the AIPES spectra of  $\text{EuNi}_2\text{P}_2$  consist of both the contributions from Eu and P terminated surfaces since the beam spot size of the present study is relatively large (about 150  $\mu\text{m}$ ) and overall spectral shapes do not depend on the beam position (not shown). It

should be noted that not all the divalent spectral weights of the surface and subsurface Eu ions inevitably contribute to the observed  $\text{Eu}^{2+}$  peak in Fig. 1(a) since the  $\text{Eu}^{2+}$  components for the pure divalent Eu ions possibly appear in the higher binding energy region and could be overlapped with the Ni  $3d$  derived peak. The bulk and subsurface spectral intensities are given by  $\exp(-d/\lambda)$  and  $1 - \exp(-d/\lambda)$ . We estimated the  $\lambda$  values to be 11 and 21 Å for  $h\nu = 500$  and 1200 eV using semiempirical expressions given in Ref. [35]. According to these formulas, the spectral intensity of the subsurface region decreases from 58% to 36% between  $h\nu = 500$  and 1200 eV. Therefore, if there exists a shift of the Eu valence value in the subsurface region, the intensity ratio between  $\text{Eu}^{2+}$  and  $\text{Eu}^{3+}$  should change dramatically as a function of photon energy. Figure 1(b) shows the AIPES spectra measured with various photon energies ranging from 500 to 1200 eV. These spectra except for  $h\nu = 1200$  eV are convoluted with a Gaussian function to compensate the differences in the energy resolutions and are normalized by the intensity of the  $\text{Eu}^{2+}$  peaks. For a quantitative analysis, we have estimated the integrated spectral weights ( $A^{\text{Eu}^{2+}}$  and  $A^{\text{Eu}^{3+}}$ ) for the  $\text{Eu}^{2+}$  ( $\text{Eu}^{3+}$ ) peaks in Fig. 1(b) by fitting them with multiple Gaussians (multiple Gaussians with a linear background) as shown in Fig. 1(c). The ratio of the spectral weights  $A^{\text{Eu}^{3+}}/A^{\text{Eu}^{2+}}$  is displayed in Fig. 1(d) and hardly depends on the photon energy within experimental uncertainty in contrast to the above calculation. Moreover, in order to reproduce the  $A^{\text{Eu}^{3+}}/A^{\text{Eu}^{2+}}$  value of 0.26 for 1200 eV, we have to assume the quite large  $d$  value of about 16 Å and that the Eu ions in the subsurface region are in an almost divalent state. Here, the photoemission cross section ratio between  $\text{Eu}^{2+}$  and  $\text{Eu}^{3+}$  and the bulk Eu valence value are set to be 7:6 and 2.5. Under this assumption, however, the  $A^{\text{Eu}^{3+}}/A^{\text{Eu}^{2+}}$  value for 500 eV is estimated to be 0.11 and inconsistent with the experimental value. From these results, we consider that the observed intensity ratio between  $\text{Eu}^{2+}$  and  $\text{Eu}^{3+}$  in Fig. 1(a) cannot simply be explained by the change of the Eu valency in the subsurface region. We also found that the intensity of Ni  $3d$  derived peak varies nonmonotonically as a function of photon energy, and this photon energy dependence could be explained by the three-dimensional nature of the Ni  $3d$  bands and the presence of the surface derived  $\text{Eu}^{2+}$  components in the same energy range.

Another possible explanation for our AIPES results is the presence of the effectively suppressed cross section for  $\text{Eu}^{3+}$  components. Note that this interpretation is consistent with our recent ARPES experiments for  $\text{EuCu}_2\text{Ge}_2$  and  $\text{EuCu}_2\text{Si}_2$  [32], which have shown that the intensity for the  $\text{Eu}^{3+}$  components for nearly trivalent  $\text{EuCu}_2\text{Si}_2$  is markedly weaker than that for the  $\text{Eu}^{2+}$  peak for nearly divalent  $\text{EuCu}_2\text{Ge}_2$  (see Fig. 1 in Ref. [32]). In addition, the weakness of the cross section for  $\text{Eu}^{3+}$  has been pointed out by resonant photoemission and x-ray absorption experiments on  $\text{EuCu}_2\text{Ge}_2$  [36]. Here, we discuss the possible mechanism for the difference in the cross sections between  $\text{Eu}^{2+}$  and  $\text{Eu}^{3+}$  components. It is well known that the many-body x-ray-absorption cross section  $w$  can be expressed by the following formula:

$$w \propto \frac{2\pi}{\hbar} |\langle \Psi_f(N) | H_{\text{int}} | \Psi_i(N) \rangle|^2 \delta(E_f - E_i - \hbar\omega), \quad (1)$$

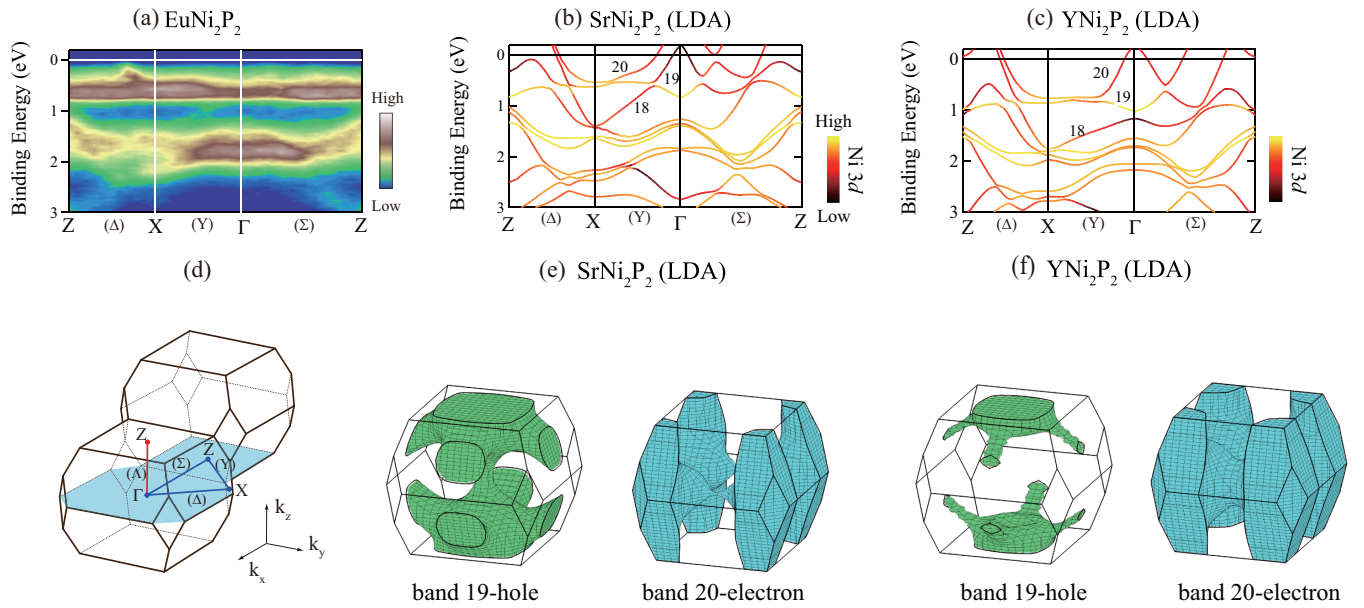


FIG. 2. (a) ARPES spectra of EuNi<sub>2</sub>P<sub>2</sub> along the high-symmetry lines measured at  $h\nu = 580$  eV. (b),(c) The corresponding calculated band structures for SrNi<sub>2</sub>P<sub>2</sub> and YNi<sub>2</sub>P<sub>2</sub>. The color of each band represents the contribution of the Ni 3d states. (d) Brillouin zone of EuNi<sub>2</sub>P<sub>2</sub>, which has a body-centered tetragonal crystal structure. (e),(f) Three-dimensional shapes of the calculated FSs of SrNi<sub>2</sub>P<sub>2</sub> and YNi<sub>2</sub>P<sub>2</sub>.

where  $|\Psi_i\rangle$  and  $|\Psi_f\rangle$  are the  $N$  electron ground and final states [37].  $H_{\text{int}}$  is the interaction operator between electrons and incident electromagnetic fields.  $E_i$ ,  $E_f$ , and  $\hbar\omega$  are the energies of the initial state, final state, and incident photons. First, we tentatively assume that the Eu 4*f* electrons are almost localized and are in a pure divalent state or a pure trivalent state, and the wave function for the 4*f* electrons can be well described by a single Slater determinant and that the photoemission process hardly affects the wave function for the remaining 4*f* and other electrons. Under this assumption, the above matrix element can be rewritten as

$$\begin{aligned} \langle \Psi_f(N) | H_{\text{int}} | \Psi_i(N) \rangle \\ = \langle \psi_f | H_{\text{int}} | \psi_i \rangle \langle \Psi_f(N-1) | \Psi_i(N-1) \rangle. \end{aligned} \quad (2)$$

The  $N$  electron matrix element is therefore factorized into the product of two matrix elements. The one-electron matrix element  $\langle \psi_f | H_{\text{int}} | \psi_i \rangle$  represents the photoemission process from the 4*f* state to the wave function of the photoelectron  $|\psi_f\rangle$ , which can be well approximated by a plane wave state in the soft x-ray range. The second matrix element denotes the overlap integral for the remaining 4*f* electrons and should be close to unity under the above assumption. In this circumstance, the photoemission intensity is proportional to  $w$  in Eq. (1), and intensities of the Eu<sup>2+</sup> and Eu<sup>3+</sup> components would be nearly the same if the one-electron matrix elements are similar in magnitude between these components. However, this assumption is clearly invalid for the Eu 4*f* electrons since the second matrix element cannot be assumed as unity because of the strong onsite Coulomb interaction. In fact, the previously proposed formula for photoemission intensities for localized 4*f* electrons, in which the 4*f* electrons are described in an intermediate scheme between the *LS* and *j-j* couplings, has a much more complicated structure [38]. Moreover, the electronic occupation of the Eu 5*d* orbital is considered to be

different between initial and final states because of the intra-atomic Coulomb interaction, and this difference also affects the photoemission cross sections. Therefore, the intensities of Eu<sup>2+</sup> and Eu<sup>3+</sup> components cannot be simply understood by the above mentioned one-electron matrix element, and the weak intensity of the Eu<sup>3+</sup> components in Fig. 1 could be reproduced by a calculation beyond the one-electron approximation. However, we are not going to further discuss this issue since such a theoretical analysis is out of the scope of the present study. Therefore, at present stage, it is difficult to conclude that whether the observed intensity ratio between Eu<sup>2+</sup> and Eu<sup>3+</sup> originates from the suppressed cross section for Eu<sup>3+</sup>. This is also because this interpretation contradicts with the majority of the previously performed photoemission experiments on Eu-based compounds, in which the photoemission cross sections for Eu<sup>2+</sup> and Eu<sup>3+</sup> are usually assumed to be the same. Because of this difficulty of estimating the accurate photoemission cross sections for Eu 4*f* components, we do not try to estimate the Eu valence of EuNi<sub>2</sub>P<sub>2</sub> from the intensity ratio between the Eu<sup>2+</sup> and Eu<sup>3+</sup> components.

To further investigate the intermediate-valence state of EuNi<sub>2</sub>P<sub>2</sub>, we performed ARPES experiments. Figure 2(a) shows the intensity plot of the ARPES spectra measured at  $h\nu = 580$  eV along the high-symmetry lines in the Brillouin zone [Fig. 2(d)]. This photon energy corresponds to the  $k_z$  value of  $\sim 19$  (in units of  $2\pi/c$ ), and momentum scans in the  $k_x$ - $k_y$  plane were conducted by changing the emission angles of photoelectrons. The spectra are normalized by the area of each energy distribution curve. The dispersive bands with strong intensities seen at around 1.8 eV are Ni 3*d* derived bands. The flat spectral feature at around 0.6 eV is due to the Eu<sup>2+</sup> components, which seem to coexist with several dispersive bands.

For comparison, we carried out band structure calculations based on a full potential version of a Dirac-type linearized



augmented plane wave method within a local density approximation (LDA) [39]. It has been confirmed by ARPES and dHvA experiments that the band structure and Fermi surfaces (FSs) of nearly divalent and trivalent Eu-based compounds are well reproduced by the band structure calculations for corresponding Sr- and Y-based compounds, respectively [32,40]. Meanwhile, the choice of a suitable non- $4f$  reference system for  $\text{EuNi}_2\text{P}_2$  is not trivial because of its intermediate-valence character. Therefore, we compare our ARPES results with both calculations for  $\text{SrNi}_2\text{P}_2$  and  $\text{YNi}_2\text{P}_2$ . In these calculations, the experimental lattice constants for  $\text{EuNi}_2\text{P}_2$  were used [34]. Figures 2(b) and 2(c) show the calculated band structures for  $\text{SrNi}_2\text{P}_2$  and  $\text{YNi}_2\text{P}_2$ , and the contribution of Ni  $3d$  states is represented by color scale. Both calculations predict the presence of several bands with a dominant Ni  $3d$  character at around 2 eV, which seem to agree well with the ARPES results. On the other hand, calculated band structures near the  $E_F$  region markedly differ between them. This difference is ascribed to an additional valence electron in  $\text{YNi}_2\text{P}_2$  compared to  $\text{SrNi}_2\text{P}_2$ . Our calculations show that the valence bands of  $\text{YNi}_2\text{P}_2$  have enhanced Y  $4d$  weight compared to the Sr  $4d$  weight for the valence bands of  $\text{SrNi}_2\text{P}_2$  (not shown). This is because Y  $4d$  state of  $\text{YNi}_2\text{P}_2$  is selectively shifted toward the higher-binding-energy side by the increased charge of the core of the Y atoms. Here, note that the difference in the band structures between  $\text{SrNi}_2\text{P}_2$  and  $\text{YNi}_2\text{P}_2$  cannot be understood by a simple rigid band model since the shapes of calculated bands 18 and 19 at around the  $\Gamma$  point are markedly different between these compounds. As shown in Figs. 2(e) and 2(f), their FSs are therefore different from each other;  $\text{SrNi}_2\text{P}_2$  is a compensated metal with an equal volume of electron and hole FSs, while  $\text{YNi}_2\text{P}_2$  is an uncompensated metal, and its electron FS becomes larger than the hole FS.

In the following, we compare the ARPES spectra with the band structure calculations near the  $E_F$  region where the calculations for  $\text{SrNi}_2\text{P}_2$  and  $\text{YNi}_2\text{P}_2$  predict different band structures. Figure 3(a) shows the ARPES spectra along the X- $\Gamma$ -X line measured at around  $h\nu = 650$  eV. We normalize these spectra by the area of each momentum distribution curve (MDC). This normalization allows us to investigate the structure of dispersive bands, because the weakly dispersive  $\text{Eu}^{2+}$  components are suppressed. The Fermi-edge-cutoff effect is also removed under this normalization. Several highly dispersive bands can be seen in the ARPES spectra. Note that these dispersive bands are considered to be hybridized with  $\text{Eu}^{2+}$  components, as observed in the previous high-energy-resolution ARPES study [23], but the valence-band splitting due to the hybridization is not resolved by the energy resolution of the present study. As shown in Fig. 3(a), there exists a parabolic spectral feature at the X point, which exhibits a minimum at around 0.6 eV. We found that this spectral feature consists of two different bands, as indicated by the red dashed lines on the left-hand side of this figure. The MDC spectrum obtained by integrating the ARPES data within 0.2 eV to  $E_F$  is shown in the upper panel of Fig. 3(a), and the presence of two distinct peaks confirms the existence of the two different bands (indicated by arrows). These two bands are not clearly resolved in the right-hand side of Fig. 3(a). However, the parabolic spectral feature in the right-hand side broadens along the momentum direction

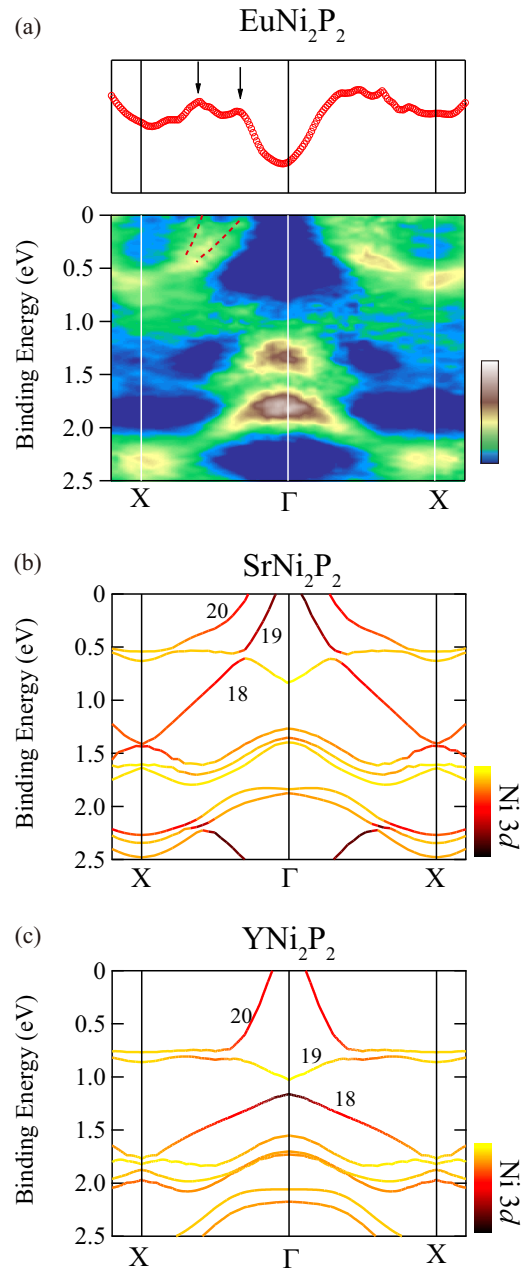


FIG. 3. (a) ARPES spectra of  $\text{EuNi}_2\text{P}_2$  measured at around  $h\nu = 650$  eV along the X- $\Gamma$ -X line. The red dashed lines are guides to eyes. The upper panel shows the MDC spectrum obtained by integrating the ARPES data within 0.2 eV to  $E_F$ . (b),(c) The corresponding calculated band structures of  $\text{SrNi}_2\text{P}_2$  and  $\text{YNi}_2\text{P}_2$ . The color scale shows the contribution of Ni  $3d$  states.

and exhibits a broad peak in the MDC spectrum shown in the upper panel. These observations are consistent with the existence of the two distinct bands. Figures 3(b) and 3(c) show the calculated band structures for  $\text{SrNi}_2\text{P}_2$  and  $\text{YNi}_2\text{P}_2$  along the same symmetry line, respectively. The two  $E_F$  crossing bands mentioned above agree well with calculated bands 19 and 20 for  $\text{SrNi}_2\text{P}_2$ , while the calculation for  $\text{YNi}_2\text{P}_2$  predicts only one  $E_F$  crossing band and, therefore, is inconsistent with the experimental band structure. Moreover, the calculation for  $\text{SrNi}_2\text{P}_2$  seems to provide a better explanation for the exper-

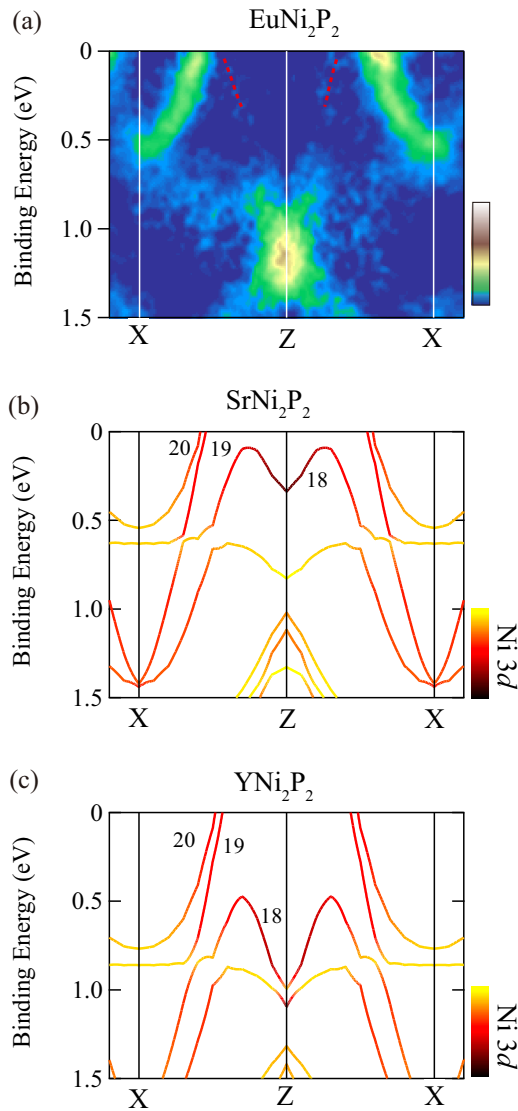


FIG. 4. (a) ARPES spectra of  $\text{EuNi}_2\text{P}_2$  measured at  $h\nu = 580$  eV along the X-Z-X line. The red dashed lines are guides to eyes. (b),(c) The corresponding calculated band structures of  $\text{SrNi}_2\text{P}_2$  and  $\text{YNi}_2\text{P}_2$ . The contribution of Ni 3d states is represented by the color scale.

imental band structure below 0.6 eV than the calculation for  $\text{YNi}_2\text{P}_2$ ; all the experimental spectral features below 0.6 eV have a correspondence with the calculated bands of  $\text{SrNi}_2\text{P}_2$ , although the bandwidth of calculated band 18 appears to be narrower in the ARPES spectra.

To further investigate the correspondence between the ARPES spectra and the calculations, we compare experimental and theoretical band structures along another symmetry line. Figure 4(a) shows the ARPES spectra of  $\text{EuNi}_2\text{P}_2$  along the X-Z-X line measured at  $h\nu = 580$  eV. The method for normalization of the ARPES spectra is the same as that in Fig. 3(a). The corresponding calculated band structures are displayed in Figs. 4(b) and 4(c). In the ARPES spectra, a parabolic spectral feature, whose bottom is located at around 0.5 eV, is observed at the X point. Calculated bands 19 and 20 for  $\text{SrNi}_2\text{P}_2$  seem to give a better agreement with this spectral

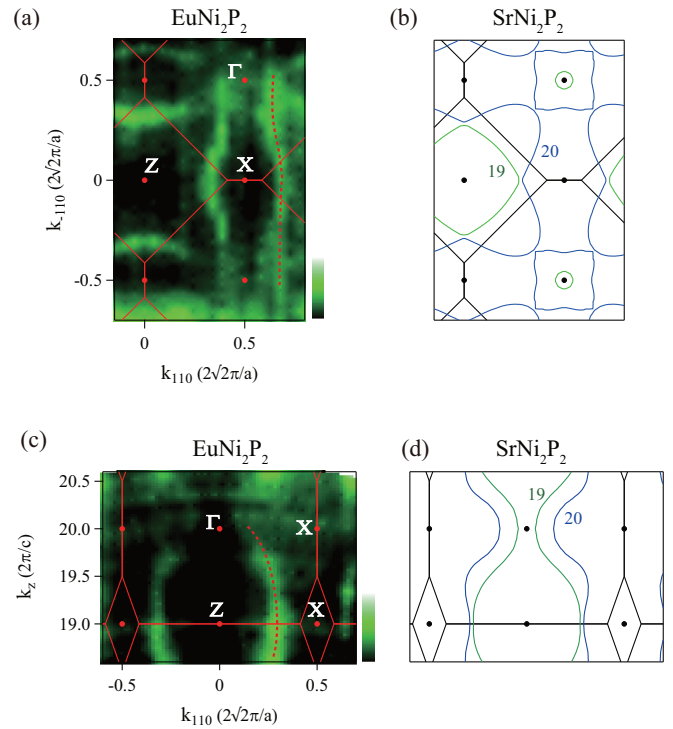


FIG. 5. (a) The photoemission intensity near  $E_F$  region in the  $k_x$ - $k_y$  plane for  $\text{EuNi}_2\text{P}_2$ . This intensity map is obtained by integrating ARPES spectra at  $h\nu = 580$  eV over  $E_F \pm 50$  meV. (c) Same intensity map in the  $k_{xy}$ - $k_z$  plane obtained by  $h\nu$ -dependent ARPES measurements. (b),(d) Corresponding calculated FSs of  $\text{SrNi}_2\text{P}_2$  in these planes.

feature than bands 19 and 20 for  $\text{YNi}_2\text{P}_2$  since the bottom positions of the calculated bands for  $\text{YNi}_2\text{P}_2$  are deeper than the experimental one. In addition, there are other dispersive experimental bands near the  $E_F$  region, as indicated by the red dashed lines in Fig. 4(a). These bands seem to correspond to calculated band 18 for  $\text{SrNi}_2\text{P}_2$ , but calculated band 18 for  $\text{YNi}_2\text{P}_2$  is located at much deeper binding energies. Moreover, as illustrated in the following paragraph, we also found that the photoemission intensity at  $E_F$  can well be explained by the calculated FSs for  $\text{SrNi}_2\text{P}_2$ . Based on these results, we conclude that the calculation for  $\text{SrNi}_2\text{P}_2$  provides a better description for the experimental band structure of  $\text{EuNi}_2\text{P}_2$ .

Figure 5(a) shows the photoemission intensity integrated over  $E_F \pm 50$  meV in the  $k_x$ - $k_y$  plane, obtained by ARPES measurements at  $h\nu = 580$  eV. We observed a characteristic intensity pattern extending parallel to the  $k_{xy}$  direction as marked by the red dashed line. Figure 5(c) displays the same intensity map in the  $k_{xy}$ - $k_z$  plane obtained by  $h\nu$ -dependent ARPES measurements. As indicated by the red dashed line in Fig. 5(c), a corrugated spectral intensity extends along the  $k_z$  direction. These intensity maps show the cross sections of the FSs if the energy resolution is high enough to resolve the shapes of individual  $E_F$  crossing bands. By considering the heavy-fermion nature of  $\text{EuNi}_2\text{P}_2$ , it is not trivial whether these intensity maps properly reflect its FS structure. Therefore, we will discuss this point later in this paper. We found that the above mentioned spectral intensity maps can well

be explained by the calculated FSs for  $\text{SrNi}_2\text{P}_2$ , which are shown in Figs. 5(b) and 5(d). The calculated FSs of band 20 in Fig. 5(b) seem to correspond to the spectral intensity marked by the red dashed line in Fig. 5(a). The FSs of band 19 are not clearly seen in Fig. 5(a), and the absence of these FSs is most likely due to the weakness of the corresponding  $E_F$  crossing bands. The corrugated intensity extending along the  $k_z$  direction in Fig. 5(c) can be explained by the FSs of bands 19 and/or 20. Although we could not resolve two individual FSs in Fig. 5(c), we have observed two  $E_F$  crossing bands around the  $\Gamma$  point, as seen in Fig. 3(a), implying that this observed corrugated intensity is ascribed not to a single FS but to both FSs of bands 19 and 20. Hence, the photoemission intensity in the vicinity of  $E_F$  can also be well explained by the calculation for  $\text{SrNi}_2\text{P}_2$ .

In the following, we discuss the physical implications of the agreement between the experimental band structure of  $\text{EuNi}_2\text{P}_2$  and the calculated results for  $\text{SrNi}_2\text{P}_2$  revealed by the present ARPES study.  $\text{EuNi}_2\text{P}_2$  is a heavy-fermion system whose electronic specific heat coefficient is largely enhanced ( $\gamma \sim 100 \text{ mJ K}^{-2} \text{ mol}^{-1}$ ), as stated in the Introduction [18,19]. In contrast, the theoretical  $\gamma$  value for  $\text{SrNi}_2\text{P}_2$  (LDA) is only  $5.2 \text{ mJ K}^{-2} \text{ mol}^{-1}$ . In fact, the effective masses  $m^*$  of calculated bands 19 and 20 in Figs. 3(b) and 4(b) are very small and estimated to be  $0.5 \sim 2 m^*/m_0$  at  $E_F$ , where  $m_0$  is the free electron mass. Corresponding experimental  $E_F$  crossing bands in Figs. 3(a) and 4(a) apparently have similar effective masses and can hardly explain the  $\gamma$  value of  $\text{EuNi}_2\text{P}_2$ . Therefore, it is considered that the observed  $E_F$  crossing bands are hybridized with the  $\text{Eu}^{2+}$  components to form heavy-fermion bands in the very vicinity of  $E_F$ , and the FSs should be reconstructed. The actual FSs of  $\text{EuNi}_2\text{P}_2$  are thus considered to be largely different from the experimental intensity maps shown in Figs. 5(a) and 5(c) as well as the calculated FSs for  $\text{SrNi}_2\text{P}_2$ . The absence of this FS reconstruction in our ARPES results is most likely due to the insufficient energy resolution and the weak photoemission intensity of the  $\text{Eu}^{2+}$  components located in the very vicinity of  $E_F$ , which would suppress the intensity of the heavy-fermion bands. On the other hand, we can safely conclude from our ARPES results that the band structure of  $\text{EuNi}_2\text{P}_2$  up to just below  $E_F$  is similar to that of  $\text{SrNi}_2\text{P}_2$ . This situation is reminiscent of Ce-based heavy-fermion systems whose band structures are often very similar to those of non-4*f* compounds, except for the very vicinity of  $E_F$  [41,42].

We shall further discuss the FS reconstruction suggested by the above argument from a different perspective. Electrical resistivity and Mössbauer experiments under pressure have revealed that the Eu valence of  $\text{EuNi}_2\text{P}_2$  continuously

evolves toward a nearly trivalent state by applying pressure [34,43]. No phase transition is observed in this process, and the Fermi-liquid character seen in low-temperature resistivity data persists in a whole-pressure range. It has been shown by de Haas-van Alphen and ARPES measurements that the band structure and FSs of nearly trivalent Eu compounds are approximately explained by the band structure calculations for corresponding Y- or La-based compounds [32,40,44,45]. Therefore, the FSs of  $\text{EuNi}_2\text{P}_2$  in the high-pressure region are considered to be similar not to the FSs of  $\text{SrNi}_2\text{P}_2$  but to the FSs of  $\text{YNi}_2\text{P}_2$ . It is generally believed that the total volume of FSs in paramagnetic states for Ce- and Yb-based heavy-fermion compounds remains unaffected by pressure, as long as the electronic state does not exhibit any transition. This is because the invariance of the volume of FSs in a Fermi liquid state is guaranteed by the Luttinger theorem [46]. If we assume that the FS volume of  $\text{EuNi}_2\text{P}_2$  is also unaffected by pressure as in Ce- and Yb-based compounds, the FS volume of  $\text{EuNi}_2\text{P}_2$  at ambient pressure is the same as that of  $\text{YNi}_2\text{P}_2$ . Thus, if this assumption is valid, the above mentioned FS reconstruction in the very vicinity of  $E_F$  should be present to enlarge the FS volume of  $\text{EuNi}_2\text{P}_2$  up to the FS volume of  $\text{YNi}_2\text{P}_2$ .

#### IV. CONCLUSION

We investigated the electronic structure of the intermediate-valence compound  $\text{EuNi}_2\text{P}_2$  by soft x-ray photoemission spectroscopy. Both the  $\text{Eu}^{2+}$  and  $\text{Eu}^{3+}$  components coexist in the AIPES spectrum, which confirms the intermediate-valence character of Eu ions. The three-dimensional band structure of  $\text{EuNi}_2\text{P}_2$  was studied by ARPES measurements, and the results were compared with the band structure calculations for the non-4*f* reference compounds  $\text{SrNi}_2\text{P}_2$  and  $\text{YNi}_2\text{P}_2$ . It was found that the band structure of  $\text{EuNi}_2\text{P}_2$  up to just below  $E_F$  is better explained by the calculation for  $\text{SrNi}_2\text{P}_2$ . The heavy-fermion bands are considered to be formed through the hybridization between dispersive bands, which resemble those for  $\text{SrNi}_2\text{P}_2$ , and the  $\text{Eu}^{2+}$  components in the very vicinity of  $E_F$ . We discuss that if the Luttinger theorem is applicable for  $\text{EuNi}_2\text{P}_2$ , the total FS volume of  $\text{EuNi}_2\text{P}_2$  should be enlarged by the formation of heavy-fermion bands up to the FS volume of  $\text{YNi}_2\text{P}_2$ .

#### ACKNOWLEDGMENTS

This work was performed under Proposal No. 2019B3811 at SPring-8 BL23SU. The present work was financially supported by JSPS KAKENHI Grants No. JP18H04329 and No. JP18K03553.

- 
- [1] A. T. Holmes, D. Jaccard, and K. Miyake, *Phys. Rev. B* **69**, 024508 (2004).
  - [2] H. Q. Yuan, F. M. Grosche, M. Deppe, C. Geibel, G. Sparn, and F. Steglich, *Science* **302**, 2104 (2003).
  - [3] K. Miyake and S. Watanabe, *J. Phys. Soc. Jpn.* **83**, 061006 (2014).
  - [4] K. Miyake and S. Watanabe, *Philos. Mag. B* **97**, 3495 (2017).
  - [5] Y. Ōnuki, M. Hedo, and F. Honda, *J. Phys. Soc. Jpn.* **89**, 102001 (2020).
  - [6] A. Mitsuda, S. Hamano, N. Araoka, H. Yayama, and H. Wada, *J. Phys. Soc. Jpn.* **81**, 023709 (2012).
  - [7] F. Honda, K. Okauchi, A. Nakamura, D. Li, D. Aoki, H. Akamine, Y. Ashitomi, M. Hedo, T. Nakama, and Y. Ōnuki, *J. Phys. Soc. Jpn.* **85**, 063701 (2016).

- [8] H.-J. Hesse, R. Lubbers, M. Winzenick, H. Neuling, and G. Wortmann, *J. Alloys Compd.* **246**, 220 (1997).
- [9] A. Nakamura, T. Nakama, K. Uchima, N. Arakaki, C. Zukeran, S. Komesu, M. Takeda, Y. Takaesu, D. Nakamura, M. Hedo, K. Yagasaki, and Y. Uwatoko, *J. Phys.: Conf. Ser.* **400**, 032106 (2012).
- [10] G. Dionicio, H. Wilhelm, Z. Hossain, and C. Geibel, *Physica B* **378-380**, 724 (2006).
- [11] A. Nakamura, T. Uejo, F. Honda, T. Takeuchi, H. Harima, E. Yamamoto, Y. Haga, K. Matsubayashi, Y. Uwatoko, M. Hedo, T. Nakama, and Y. Ōnuki, *J. Phys. Soc. Jpn.* **84**, 124711 (2015).
- [12] S. Doniach, *Physica B* **91**, 231 (1977).
- [13] M. Nakashima, Y. Amako, K. Matsubayashi, Y. Uwatoko, M. Nada, K. Sugiyama, M. Hagiwara, Y. Haga, T. Takeuchi, A. Nakamura, H. Akamine, K. Tomori, T. Yara, Y. Ashitomi, M. Hedo, T. Nakama, and Y. Ōnuki, *J. Phys. Soc. Jpn.* **86**, 034708 (2017).
- [14] S. Fukuda, Y. Nakanuma, J. Sakurai, A. Mitsuda, Y. Isikawa, F. Ishikawa, T. Goto, and T. Yamamoto, *J. Phys. Soc. Jpn.* **72**, 3189 (2003).
- [15] Z. Hossain, C. Geibel, N. Senthilkumaran, M. Deppe, M. Baenitz, F. Schiller, and S. L. Molodtsov, *Phys. Rev. B* **69**, 014422 (2004).
- [16] W. Iha, T. Yara, Y. Ashitomi, M. Kakihana, T. Takeuchi, F. Honda, A. Nakamura, D. Aoki, J. Gouchi, Y. Uwatoko, T. Kida, T. Tahara, M. Hagiwara, Y. Haga, M. Hedo, T. Nakama, and Y. Ōnuki, *J. Phys. Soc. Jpn.* **87**, 064706 (2018).
- [17] R. Nagarajan, G. K. Shenoy, L. C. Gupta, and E. V. Sampathkumaran, *Phys. Rev. B* **32**, 2846 (1985).
- [18] Y. Hiranaka, A. Nakamura, M. Hedo, T. Takeuchi, A. Mori, Y. Hirose, K. Mitamura, K. Sugiyama, M. Hagiwara, T. Nakama, and Y. Ōnuki, *J. Phys. Soc. Jpn.* **82**, 083708 (2013).
- [19] R. A. Fisher, P. Radhakrishna, N. E. Phillips, J. V. Badding, and A. M. Stacy, *Phys. Rev. B* **52**, 13519 (1995).
- [20] N. Higa, M. Yogi, H. Kuroshima, T. Toji, H. Niki, Y. Hiranaka, A. Nakamura, T. Nakama, M. Hedo, and Y. Ōnuki, *J. Phys. Soc. Jpn.* **87**, 094708 (2018).
- [21] Y. Hiranaka, A. Nakamura, M. Hedo, T. Takeuchi, K. Matsubayashi, Y. Uwatoko, T. Nakama, and Y. Ōnuki, *JPS Conf. Proc.* **3**, 011011 (2014).
- [22] V. Guritanu, S. Seiro, J. Sichelschmidt, N. Caroca-Canales, T. Iizuka, S. Kimura, C. Geibel, and F. Steglich, *Phys. Rev. Lett.* **109**, 247207 (2012).
- [23] S. Danzenbächer, D. V. Vyalikh, Y. Kucherenko, A. Kade, C. Laubschat, N. Caroca-Canales, C. Krellner, C. Geibel, A. V. Fedorov, D. S. Dessau, R. Follath, W. Eberhardt, and S. L. Molodtsov, *Phys. Rev. Lett.* **102**, 026403 (2009).
- [24] H. Anzai, K. Ichiki, E. F. Schwier, H. Iwasawa, K. Shimada, H. Namatame, M. Taniguchi, A. Mitsuda, H. Wada, and K. Mimura, *J. Phys.: Conf. Ser.* **807**, 012006 (2017).
- [25] A. Sekiyama, T. Iwasaki, K. Matsuda, Y. Saitoh, Y. Ōnuki, and S. Suga, *Nature (London)* **403**, 396 (2000).
- [26] S. Tanuma, C. J. Powell, and D. R. Penn, *Surf. Interface Anal.* **43**, 689 (2011).
- [27] Y. Saitoh, Y. Fukuda, Y. Takeda, H. Yamagami, S. Takahashi, Y. Asano, T. Hara, K. Shirasawa, M. Takeuchi, T. Tanaka, and H. Kitamura, *J. Synchrotron Radiat.* **19**, 388 (2012).
- [28] S.-i. Fujimori, M. Kobata, Y. Takeda, T. Okane, Y. Saitoh, A. Fujimori, H. Yamagami, Y. Matsumoto, E. Yamamoto, N. Tateiwa, and Y. Haga, *Phys. Rev. B* **96**, 125117 (2017).
- [29] F. Gerken, Ph.D. thesis, University of Hamburg (1982).
- [30] J. Yeh and I. Lindau, *At. Data Nucl. Data Tables* **32**, 1 (1985).
- [31] W. D. Schneider, C. Laubschat, G. Kalkowski, J. Haase, and A. Puschmann, *Phys. Rev. B* **28**, 2017 (1983).
- [32] I. Kawasaki, S.-i. Fujimori, Y. Takeda, H. Yamagami, W. Iha, M. Hedo, T. Nakama, and Y. Ōnuki, *Phys. Rev. B* **100**, 035111 (2019).
- [33] D. Y. Usachov, A. V. Tarasov, S. Schulz, K. A. Bokai, I. I. Tupitsyn, G. Poelchen, S. Seiro, N. Caroca-Canales, K. Kliemt, M. Mende, K. Kummer, C. Krellner, M. Muntwiler, H. Li, C. Laubschat, C. Geibel, E. V. Chulkov, S. I. Fujimori, and D. V. Vyalikh, *Phys. Rev. B* **102**, 205102 (2020).
- [34] S. A. Medvedev, P. Naumov, O. Barkalov, C. Shekhar, T. Palasyuk, V. Ksenofontov, G. Wortmann, and C. Felser, *J. Phys.: Condens. Matter* **26**, 335701 (2014).
- [35] S. Tanuma, C. Powell, and D. Penn, *Surf. Sci.* **192**, L849 (1987).
- [36] S. Banik, A. Bendounan, A. Thamizhavel, A. Arya, P. Risterucci, F. Sirotti, A. K. Sinha, S. K. Dhar, and S. K. Deb, *Phys. Rev. B* **86**, 085134 (2012).
- [37] S. Hüfner, *Photoelectron Spectroscopy*, 3rd ed. (Springer, Berlin, 2003).
- [38] F. Gerken, *J. Phys. F: Met. Phys.* **13**, 703 (1983).
- [39] H. Yamagami, *J. Phys. Soc. Jpn.* **67**, 3176 (1998).
- [40] Y. Ōnuki, A. Nakamura, D. Aoki, M. Boukahil, Y. Haga, T. Takeuchi, H. Harima, M. Hedo, and T. Nakama, *J. Phys.: Conf. Ser.* **592**, 012049 (2015).
- [41] Q. Y. Chen, X. B. Luo, E. Vescovo, K. Kaznatcheev, F. J. Walker, C. H. Ahn, Z. F. Ding, Z. H. Zhu, L. Shu, Y. B. Huang, and J. Jiang, *Phys. Rev. B* **100**, 035117 (2019).
- [42] Y. Saitoh, H. Fujiwara, T. Yamaguchi, Y. Nakatani, T. Mori, H. Fuchimoto, T. Kiss, A. Yasui, J. Miyawaki, S. Imada, H. Yamagami, T. Ebihara, and A. Sekiyama, *J. Phys. Soc. Jpn.* **85**, 114713 (2016).
- [43] B. Perscheid, E. Sampathkumaran, and G. Kaindl, *J. Magn. Magn. Mater.* **47**, 410 (1985).
- [44] A. Nakamura, T. Takeuchi, H. Harima, M. Hedo, T. Nakama, and Y. Ōnuki, *J. Phys. Soc. Jpn.* **83**, 053708 (2014).
- [45] I. Kawasaki, M. Kobata, S.-i. Fujimori, Y. Takeda, H. Yamagami, A. Nakamura, W. Iha, M. Hedo, T. Nakama, and Y. Ōnuki, *J. Phys. Soc. Jpn.* **89**, 044704 (2020).
- [46] J. M. Luttinger, *Phys. Rev.* **119**, 1153 (1960).